Desalination and Water Treatment
www.deswater.com

doi: 10.5004/dwt.2023.29637

296 (2023) 60–70
June

Photocatalytic degradation and photocatalytic hydrogen production of rambutan-like structure $In_2S_3/CaIn_2S_4$ composites

Yingru Sun[a,†], Yixuan Li[a,†], Tianyu Hu[b,*], Li Li[a,*], Yin Liu[a], Xiaoyu Dong[a], Yanzhen Cao[a]

[a]*College of Chemistry and Chemical Engineering, Qiqihar University, Qiqihar 161006, China, Tel.: +86 0452-2738200; email: qqhrll@163.com/qqhrlili@126.com (L. Li)*
[b]*College of Chemical Engineering, Zhejiang University of Technology, Hangzhou 310014, China, email: hutianyu@zjut.edu.cn (T. Hu)*

Received 14 November 2022; Accepted 12 May 2023

ABSTRACT

In this paper, $In_2S_3/CaIn_2S_4$ composites were synthesized by a programmed temperature hydrothermal method. The crystal structure, morphology, and surface physicochemical properties of $In_2S_3/CaIn_2S_4$ composites were tested by X-ray diffraction, X-ray photoelectron spectroscopy, scanning electron microscopy, UV-Visible diffuse reflectance spectroscopy, and N_2 adsorption–desorption measurements. The results show that $In_2S_3/CaIn_2S_4$ composite contains mixed phases of tetragonal phase $CaIn_2S_4$ and cubic phase In_2S_3, and has the rambutan-like structure with a favor optical absorption in visible region. Using methyl orange as the degradation object, the photocatalytic degradation experiments were carried out under ultraviolet light, visible light, and simulated sunlight. The results show that $In_2S_3/CaIn_2S_4$ composite with the molar ratio of 1:10 possesses the best photocatalyst activity. Meanwhile, the composite presents the certain extensiveness in the degradation of organic pollutants with different structures, it also has a certain photocatalytic hydrogen ability, and its photocatalytic hydrogen production activity is much higher than that of commercially available P25. In addition, based on the trapping experiments, a possible photocatalytic mechanism of $In_2S_3/CaIn_2S_4$ was proposed.

Keywords: Indium matrix composite; $In_2S_3/CaIn_2S_4$; Programmed temperature hydrothermal method; Photocatalysis; Hydrogen production

1. Introduction

With the development of the social economy and the acceleration of industrialization, energy shortage and environmental pollution have become two major problems that need to be solved urgently in the world today. In recent years, environmental pollution and energy scarcity have been major issues for human research, and scientists have developed many technologies to address these issues: (a) non-destructive methods such as adsorption, washing and membrane filtration; (b) destructive methods including photocatalysis, biodegradation and catalytic oxidation. Among them, the adsorption technology is low cost, easy to operate. However, in most cases, the adsorption efficiency is not high, and the pollutant is not completely "eliminated" or "destroyed". In addition, Fenton oxidation method has the advantages of rapid reaction, non-selectivity of oxidation, strong removal ability of organic matter, but it uses many reagents, high processing cost, and easy to produce secondary pollution [1]. Gao et al. [2] studied the photocatalytic material CA^+ with calcium alginate as the carrier and cetyltrimethylammonium bromide as the surfactant for the degradation of actual tetracycline-contaminated wastewater, and it was found that the photocatalytic material has good degradation stability, short photocatalytic degradation time and high catalytic efficiency. Rodrigues et al. [3] developed a hybrid photocatalyst consisting of TiO_2 and g-C_3N_4 for effective remediation of the persistent organic

* Corresponding authors.
† These authors contributed equally to this work and should be considered co-first authors.

pollutant 4-chlorophenol in wastewater, and results indicated that photocatalytic activity under visible light of TiO_2/g-C_3N_4 was improved by 44.8% compared to pure TiO_2. So, it is of great significance to study high efficiency photocatalysts [4,5].

As a traditional photocatalyst, TiO_2 has the characteristics of low cost, high chemical stability and non-toxicity. However, due to the limitation of band structure, the photocatalytic effect of TiO_2 under visible light is not ideal [6,7]. In addition, MOFs have attracted much attention as crystalline porous materials with customized pore/structure and potential applications in adsorption environments [8]. However, MOFs itself brittle, small solubility, not easy to form, with other materials and other characteristics, so that its advantages in function is difficult to be fully reflected [9]. Many efforts have been made to develop new materials with inherent visible-light catalytic activity, such as metal oxides, metal sulfides/oxygen sulfides, metal nitrides and metal-free photocatalysts.

At present, a large number of studies have shown that sulfides have special physical and chemical properties, such as superconductivity, charge density waves, nonlinear optics, and catalytic properties. Sulfide-based photocatalysts have the advantages of narrow band gap, visible light absorption and high photocatalytic performance, etc. [10–13]. However, binary sulfides are prone to photo-corrosion and have a limited-service life, while ternary sulfides have better stability, unique optoelectronic properties and photocatalytic properties. $CaIn_2S_4$ is a novel ternary sulfide, which is one of the cheapest alkaline earth metal-based semiconductor. $CaIn_2S_4$ has a narrow band gap (~1.9 eV), and it shows excellent photocatalytic activity. Moreover, $CaIn_2S_4$ with the hierarchical structure gives high accessible surface area, which is helpful for enhancing the adsorption quantity of water pollutants on the catalyst surface and improving the photocatalytic degradation performance. Natarajan and Tayade [14] prepared a visible light-responsive redox-mediator-free calcium indium sulfide ($CaIn_2S_4$) and bismuth tungstate-(Bi_2WO_6)-based direct dual semiconductor nanocomposites by combination of hydrothermal and wetness impregnation methods, at the same time, they confirmed that visible light response of Bi_2WO_6 was considerably enhanced, and its adsorption capacity was significantly improved after combining with $CaIn_2S_4$. Ding et al. [15] synthesized a novel single-phase nanostructured photocatalyst $CaIn_2S_4$ by post-calcination hydrothermal method. The photocatalyst exhibited considerable activity for hydrogen evolution from pure water without any sacrificial agents or cocatalysts under visible light irradiation.

However, there are few reports on the construction and synthesis of $CaIn_2S_4$-based composite photocatalysts. Similar to other narrow-band catalysts, the photocatalytic degradation efficiency of $CaIn_2S_4$ alone is very limited due to the low separation efficiency of photogenerated electron vacancies [16]. Therefore, the coupling of $CaIn_2S_4$ with other semiconductors is of great importance for effectively suppressing light-generated electron–hole pair recombination.

In recent years, although there is relatively little research on in-based nanomaterials in domestic and abroad, the excellent prospects of indium in photocatalysis have gradually attracted widespread attention. In_2S_3 is an important III–VI semiconductor photocatalytic material with a bandgap of 2.0–2.2 eV, belonging to a medium-bandwidth semiconductor, which can utilize visible light or even sunlight as a photocatalytic light source [17]. At atmospheric pressure, In_2S_3 has three kinds of defective structures: α-In_2S_3 (defect cubic), β-In_2S_3 (defect spinel), and γ-In_2S_3 (layered structure) [18]. Among them, β-In_2S_3 has a stable structure at room temperature. Due to its non-toxicity, stable performance, and absorption of the visible light band, it has been studied and applied in photocatalytic degradation of dyes, photocatalytic hydrogen production, and optoelectronic devices. Fu et al. [19] synthesized β-In_2S_3 nanobelts by solvothermal method, and found that β-In_2S_3 nanobelts had a high photocatalytic performance for the degradation of methylene blue-ethanol solution. Wang et al. [20] used a simple hydrothermal precipitation method to synthesize In_2S_3@TiO_2 nanobelt heterostructures composed of In_2S_3 nanoparticles, which could degrade methyl orange under ultraviolet and visible light. Fang et al. [21] successfully prepared an indented hexagonal In_2S_3 nanorod structure by vulcanizing MIL-68-In in a metal–organic framework precursor, and the synthesized In_2S_3-8h showed a very good effect in degrading tetracycline hydrochloride and methyl orange.

In this paper, by combining $CaIn_2S_4$ and In_2S_3, the transfer path of photogenerated electron–hole pair is extended, the separation rate of the photogenerated electron–hole of the photocatalyst is improved, and the photocatalytic activity of the composites is further improved. During the experiment, by examining the relationship between the ratio of reactants and the photocatalytic activity, the optimal charging ratio of the reactants for photocatalytic activity was finally determined. In addition, in the experiment, the as-synthesized In_2S_3/$CaIn_2S_4$ composites were used for organic dye pollutants with complex structure, high potential toxicity, and carcinogenic effect, which provides some basic data for the application of In_2S_3/$CaIn_2S_4$ composites.

2. Experimental part

2.1. Materials

Calcium nitrate ($Ca(NO_3)_2{\cdot}4H_2O$), indium nitrate ($In(NO_3)_3{\cdot}4H_2O$), thioacetamide (TAA), Tianjin sodium sulfide ($Na_2S{\cdot}9H_2O$), isopropyl alcohol (IPA), p-benzoquinone (BQ), disodium ethylenediaminetetraacetate (EDTA-2Na), methyl orange (MO), rhodamine B (RB), acid fuchsin (AF), methylene blue (MB) and phenol (PH) used in the experiments were all commercially available analytical grades, and all experimental water was double distilled water.

2.2. Preparation of In_2S_3/$CaIn_2S_4$ composites

$In(NO_3)_3{\cdot}4H_2O$, $Ca(NO_3)_2{\cdot}4H_2O$, and TAA were dissolved in double-distilled water and stirred for 20 min to obtain a clear solution. Transfer the solution to a stainless-steel autoclave lined with PTFE, hold at 120°C for 48 h, then washed several times with deionized water and ethanol, and dried at 60°C for 12 h. The obtained samples were labeled as 1:x In_2S_3/$CaIn_2S_4$ composites (1:x is molar ratio). Monomers prepared in the same method were used for comparison.

2.3. Characterization of photocatalyst

The X-ray diffraction (XRD) analysis was performed by Bruker-AXS (D8) X-ray diffractometer, Germany (Cu target Kα radiation (λ = 0.15406 nm), tube voltage 60 kV, tube current 80 mA, and scanning range 20°–80°). The X-ray photoelectron (XPS) spectrum of the sample was measured by ESCALAB250Xi X-ray photoelectron spectrometer (Mg K-ADES source residual gas pressure less than 10^{-8} Pa test). The scanning electron microscopy (SEM) analysis of the samples were performed by S-4700 scanning electron microscope, Hitachi, Japan (working voltage 5 kV). The samples were analyzed by TEM using a H-7650 transmission electron microscope from Hitachi, Japan, and the accelerating voltage was 100 kV. The UV-Vis diffuse reflection absorption spectroscopic tests of the samples were carried out by TU-1901 UV-Vis double beam spectrophotometer (integrating sphere) produced by Beijing General Analysis Co., Ltd. The specific surface area and pore size of the sample were determined by 3H-2000 specific surface area and pore size analysis instrument, Best Technology Company, Beijing (temperature 77 K). The photoluminescence (PL) spectra were recorded using fluorescence spectrophotometer (Hitachi F-7000, Japan) and the excitation wavelength was set at 400 nm. Raman spectrometer (LabRam HR Evolution; Thermo Fischer DXR) recorded the Raman spectrum at a wavelength set to 325 nm. Absorbance was determined by TU-1901 UV-Vis double beam spectrophotometer, General Analytical Company, Beijing.

2.4. Photocatalytic experiments

The photocatalytic experimental device consists of a cylindrical quartz glass sleeve and a built-in light source surrounded by quartz glass. The ultraviolet light source is a 125 W Hg lamp (the maximum emission wavelength is 313.2 nm), and the visible light source is a 400 W Xe lamp (the maximum emission spectrum is greater than 410 nm, and a glass inner sleeve is used to filter out the ultraviolet light). The light source for the simulated sunlight photocatalysis experiment was a 300 W Xe lamp (external type, with a spectral range of 320–780 nm).

The photocatalytic activity of the samples was evaluated by degrading methyl orange (MO) at a concentration of 50 mg/L. Before lighting, agitate for 30 min in the dark to achieve adsorption–desorption equilibrium. Take 3 mL of the suspension at regular intervals and centrifuge to remove the photocatalyst particles. The absorbance at λ_{max} is then determined with a UV-Vis spectrophotometer (TU-1901 type).

2.5. Photocatalytic hydrogen evolution production experiments

The photocatalytic hydrogen production experiments were carried out in a vacuum reactor connected to a closed loop system (Labsolar-III AG system). 100 mg of the photocatalyst was dispersed in 50 mL of distilled water, and 3.0 g of $Na_2S{\cdot}H_2O$ was added as sacrificial agents. Under the condition of vacuum degassing and constant stirring, the experiment of hydrogen production by photolysis of water was started. A 300 W Xe lamp was used as a light source, fixed at a distance of 10 cm from the reaction solution. High-purity nitrogen as the carrier gas, the flow rate is 0.5 mL/s; the output pressure is 0.4–0.6 MPa, and the working voltage and current are about 20 mV and 50 mA. During the reaction, the temperature of the reactor was maintained at about 5°C by circulating cooling water. By analyzing hydrogen production using online gas chromatography, the gas was collected under a certain irradiation time. The reaction was carried out for 8 h. The column was a 5 Å molecular sieve column, and the detector was a thermal conductivity detector (TCD). Based on the peak areas at different reaction times, the hydrogen production was calculated, and the catalytic activity of the photocatalyst was measured by the total hydrogen production over 8 h.

3. Results and discussion

3.1. XRD analysis

In order to investigate the crystal structure of the as-synthesized composites, a series of XRD tests were carried out. It can be seen from Fig. 1a. that as-prepared composites are mixed crystal phase of $CaIn_2S_4$ and In_2S_3. $CaIn_2S_4$ is mainly a cubic phase structure, and the diffraction peaks are located at the diffraction angles 2θ of 27.4° (311), 28.4° (222), 33.1° (400), 43.4° (511), and 47.7° (440) (JCPDS 31-0272) [22]. The peaks at 2θ values of 27.4°, 28.6°, 33.2°, 43.6°, and 47.7° correspond to the (109), (206), (00$\underline{12}$), (10$\underline{15}$), and (22$\underline{12}$)

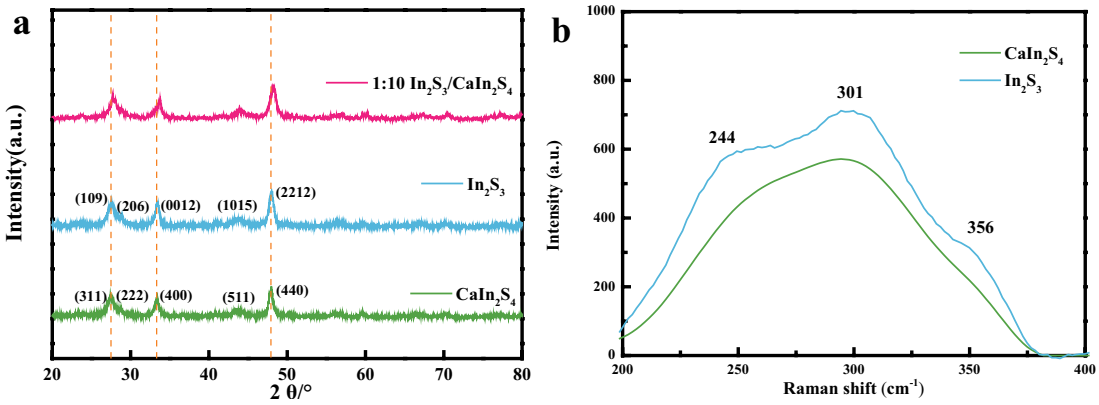

Fig. 1. X-ray diffraction patterns of $CaIn_2S_4$, In_2S_3, and 1:10 $In_2S_3/CaIn_2S_4$ (a), Raman spectra of In_2S_3 and $CaIn_2S_4$ (b).

planes of In_2S_3 tetragonal phase (JCPDS 25-0390), indicating that as-prepared sample is β-In_2S_3 crystal [23,24]. It can be clearly observed from Fig. 1a that the characteristic diffraction peak of 1:10 $In_2S_3/CaIn_2S_4$ is slightly shifted from the characteristic diffraction peak of $CaIn_2S_4$ monomer and In_2S_3 monomer, indicating that $CaIn_2S_4$ and In_2S_3 have been compounded, moreover, as-prepared 1:10 $In_2S_3/CaIn_2S_4$ composite contains $CaIn_2S_4$ and In_2S_3 mixed crystal phases [25]. Raman spectroscopy was employed to investigate the fingerprint vibrations and the formation of In_2S_3, and the results are illustrated in Fig. 1b. The Raman spectrum of In_2S_3 exhibits three distinct peaks at 244, 301, and 356 cm^{-1}. The peak at 301 cm^{-1} appears due to the A_{4g} mode, whereas the peaks at 244 and 356 cm^{-1} indicates the A_{1g} and A_{2g} modes, respectively. The A_{1g}, A_{2g}, and A_{4g} modes affirm the creation of the tetragonal β-In_2S_3 phase, which agrees well with the XRD results. At 244, 301, and 356 cm^{-1}, there is no obvious peak for $CaIn_2S_4$, which is enough to explain the difference between the two substances [26].

The crystallite size (D^*) of each sample can be obtained by calculating by the Scherrer formula, and the specific values are listed in Table 1. It can be seen from Table 1 that the crystallite size of $CaIn_2S_4$ and In_2S_3 becomes larger after compounding. According to reports, the larger crystallite size can effectively improve its photocatalytic activity, which is consistent with the results of ultraviolet photocatalytic experiments [27].

3.2. SEM and TEM analysis

In order to explore the morphological characteristics of $In_2S_3/CaIn_2S_4$ composites, SEM and TEM analysis of $In_2S_3/CaIn_2S_4$ composites were carried out, and the results are shown in Fig. 2. It can be clearly observed from Fig. 2a that the synthesized 1:10 $In_2S_3/CaIn_2S_4$ composite is in the shape of rambutan, the size is relatively uniform, about 1.2–1.5 μm, and the surface has a large number of irregular strips. The prepared composite material is expected to have a larger specific surface area and a larger contact area with the reactants, which is expected to improve its photocatalytic activity. Fig. 2b is the TEM image of the $In_2S_3/CaIn_2S_4$ composite material. It can be observed that the shape in the figure is almost the same as that of SEM image.

Table 1
Crystallite size of $CaIn_2S_4$, In_2S_3, and 1:10 $In_2S_3/CaIn_2S_4$

Sample	D^* (nm)
$CaIn_2S_4$	16.7
In_2S_3	7.5
1:10 $In_2S_3/CaIn_2S_4$	17.2

3.3. XPS analysis

The element composition and chemical valence state in the $In_2S_3/CaIn_2S_4$ composites are analyzed by XPS, as shown in Fig. 3. Fig. 3a shows the XPS spectra of $In_2S_3/CaIn_2S_4$, In_2S_3 and $CaIn_2S_4$. It can be seen that the spectrum of $In_2S_3/CaIn_2S_4$ contains Ca, In, S, O and C elements, the C may be caused by the hydrocarbons in the instrument itself, and the O may be adsorbed oxygen [28]. Fig. 3b shows the XPS spectra of Ca $2p_{3/2}$ and Ca $2p_{1/2}$, with binding energies of 347.6 and 351.2 eV, respectively, indicating that Ca exists in the form of Ca^{2+} [29,30]. Compared with $CaIn_2S_4$, the binding energy of the Ca $2p_{3/2}$ (347.6 eV) and Ca $2p_{1/2}$ (351.2 eV) orbitals at 1:10 $In_2S_3/CaIn_2S_4$ is transferred to lower energy by 0.3 eV, respectively. Fig. 3c shows the XPS spectra of In $3d_{5/2}$ and In $3d_{3/2}$, and the corresponding binding energies are 443.7 and 451.3 eV, respectively, indicating that In exists in the form of In^{3+} [31,32]. Compared to In_2S_3 and $CaIn_2S_4$, the binding energies of In $3d_{5/2}$ (443.7 eV) and In $3d_{3/2}$ (453.1 eV) at 1:10 $In_2S_3/CaIn_2S_4$ shift slightly to lower values. Fig. 3d shows the XPS spectra of S $2p_{3/2}$ and S $2p_{1/2}$, the corresponding binding energies are 160.8 and 161.8 eV, respectively, indicating that S exists in the S^{2-} valent [33]. The binding energy of 1:10 $In_2S_3/CaIn_2S_4$ composites In $3d_{5/2}$ (443.7 eV) and In $3d_{3/2}$ (453.1 eV) decreases slightly compared with In_2S_3 and $CaIn_2S_4$. The slight changes in the binding energies of elements such as Ca, In, and S also confirm the effective electronic interaction between In_2S_3 and $CaIn_2S_4$ in $In_2S_3/CaIn_2S_4$ composites.

3.4. UV-Visible diffuse reflectance spectroscopy analysis

In order to explore the effect of the combination of the two monomers on the light absorption properties, UV-Visible diffuse reflectance spectroscopy measurements were carried out, and the results are shown in Fig. 4. Fig. 4a shows the absorption spectra of $In_2S_3/CaIn_2S_4$ composites with different ratios prepared by a programmed temperature hydrothermal method. It can be clearly observed that $In_2S_3/$

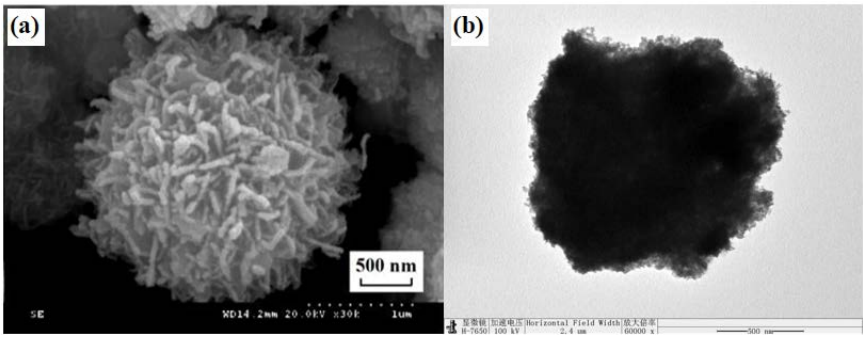

Fig. 2. Scanning and transmission electron microscopy images of $In_2S_3/CaIn_2S_4$ (a and b).

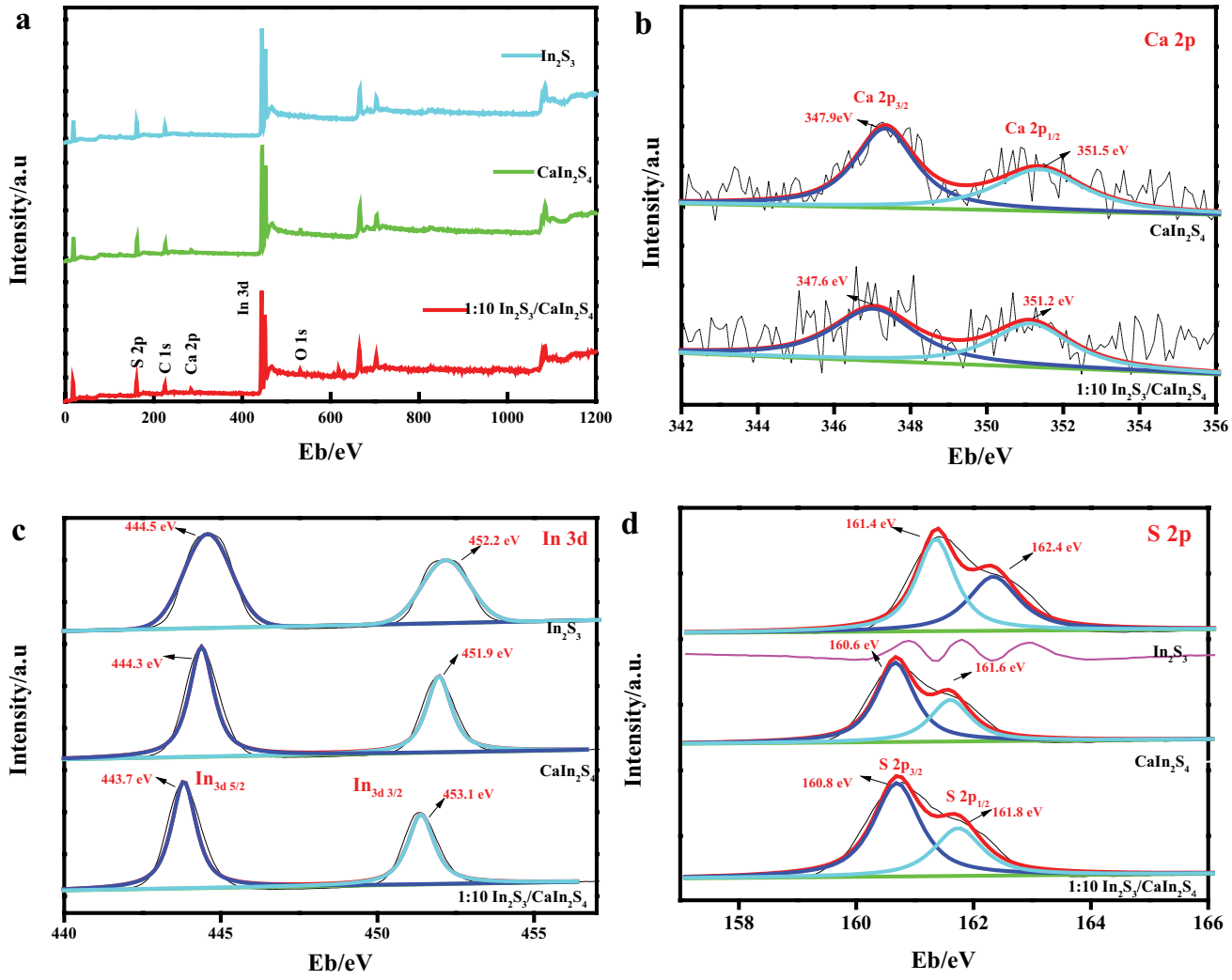

Fig. 3. X-ray photoelectron spectroscopy survey spectra of $In_2S_3/CaIn_2S_4$, In_2S_3 and $CaIn_2S_4$ (a), the high-resolution X-ray photoelectron spectroscopy spectra of Ca 2p (b), In 3d (c), and S 2p (d).

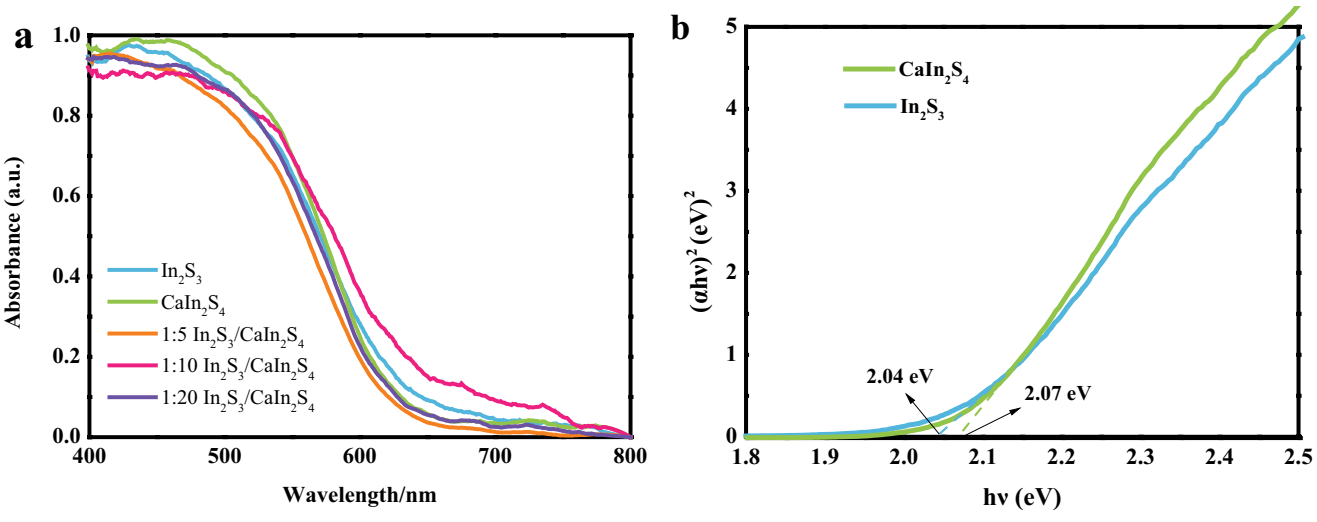

Fig. 4. UV-Visible diffuse reflectance spectroscopy (a) and Kubelka–Munk energy curve plots of different samples (b).

$CaIn_2S_4$ composites have strong absorption in the visible light region, moreover, 1:10 $In_2S_3/CaIn_2S_4$ has the strongest visible light absorption capacity.

Based on the optical absorption results of the UV-Vis diffuse reflectance spectra of all samples, the bandgap energy of the samples is calculated by the following formula [34]:

$$\left(\alpha h\nu\right)^2 = K\left(h\nu - E_g\right) \quad (1)$$

where α is the absorption coefficient, K is the parameter related to the valence band and conduction band, when n = 2, it is the indirect bandgap, hν is the absorbed energy, and E_g is the bandgap energy.

3.5. N_2 adsorption–desorption measurement

In order to investigate the adsorption–desorption isotherm type, pore size distribution, specific surface area, total pore volume, and average pore size of $In_2S_3/CaIn_2S_4$, the N_2 adsorption–desorption measurements were carried out for $CaIn_2S_4$, In_2S_3, and 1:10 $In_2S_3/CaIn_2S_4$, the related results are shown in Fig. 5 and Table 2. It can be observed from adsorption–desorption isotherm that under higher relative pressure, the condensation section of the capillary is relatively steep, and after condensation occurs in all pores, the adsorption only occurs on the outer surface which is much smaller than the surface area, and the curve gradually tends to be flat. According to IUPAC classification, the N_2 adsorption–desorption isotherms of $CaIn_2S_4$, In_2S_3 and 1:10 $In_2S_3/CaIn_2S_4$ are type IV isotherms with hysteresis loops, which indicates that 1:10 $In_2S_3/CaIn_2S_4$ belongs to mesoporous materials [35,36]. The hysteresis loop of 1:10 $In_2S_3/CaIn_2S_4$ belongs to the H3 type hysteresis loop, and the type of isotherm and hysteresis loop is caused by the coagulation of capillaries and the aggregation of particles in the structure [37,38].

It can be seen from Table 2 that the 1:10 $In_2S_3/CaIn_2S_4$ composites have a larger specific surface area, indicating that the photocatalyst surface has a larger contact area with the dye and provides more active sites, which is more conducive to the degradation reaction. It can be observed from the BJH pore size distribution curve inset in Fig. 5, the pore size distributions of the composites and monomers are relatively uniform. It is attributed to the relatively mild programmed temperature hydrothermal synthesis process, which makes the internal structure of the photocatalyst relatively uniform.

The specific surface area of the 1:10 $In_2S_3/CaIn_2S_4$ composite are larger than $CaIn_2S_4$, which indicates that the performance of the composite based on the $CaIn_2S_4$ structure has been optimized, indicating that the 1:10 $In_2S_3/CaIn_2S_4$ photocatalyst will have better photocatalytic activity, which is consistent with the results of photocatalytic experiments under ultraviolet light.

3.6. Photoluminescence analysis

In order to study the separation of electron–hole pairs of $In_2S_3/CaIn_2S_4$ composites, PL analysis was performed on different samples. It can be seen from Fig. 6a and b that under the excitation of 400 nm, 1:10 $In_2S_3/CaIn_2S_4$ has the lowest PL intensity compared with the samples of monomeric In_2S_3, monomeric $CaIn_2S_4$, and other ratios [39]. This result shows that the prepared 1:10 $In_2S_3/CaIn_2S_4$ has a significant inhibitory effect on the recombination of photogenerated electrons and holes, which further indicates that the synergistic effect of In_2S_3 and $CaIn_2S_4$ can enhance the transfer of photogenerated carriers in the composite material, improve the separation efficiency of photogenerated electrons and holes, thereby prolonging the lifetime of photogenerated electrons.

3.7. Photocatalytic performance

In order to investigate the photocatalytic performance of the as-synthesized samples, photocatalytic experiments were carried out, and the results are shown in Fig. 7. It can be seen from Fig. 7a and b that the MO is directly photodegraded for 15 min under ultraviolet light irradiation,

Table 2
Specific surface area, pore volume, and average pore size of $CaIn_2S_4$, In_2S_3, and $In_2S_3/CaIn_2S_4$

Sample	S_{BET} (m^2/g)	V_{total} (cm^3/g)	D (nm)
$CaIn_2S_4$	61.3	0.262	11.1
In_2S_3	62.2	0.232	14.9
1:10 $In_2S_3/CaIn_2S_4$	66.1	0.164	9.9

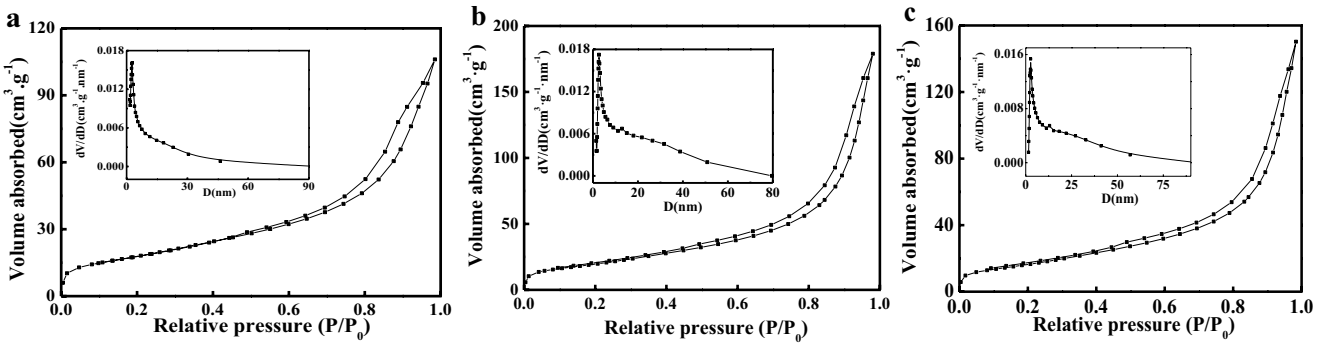

Fig. 5. N_2 adsorption–desorption isotherm and pore-size distribution curve (illustration) of 1:10 $In_2S_3/CaIn_2S_4$ (a), $CaIn_2S_4$ (b), and In_2S_3 (c).

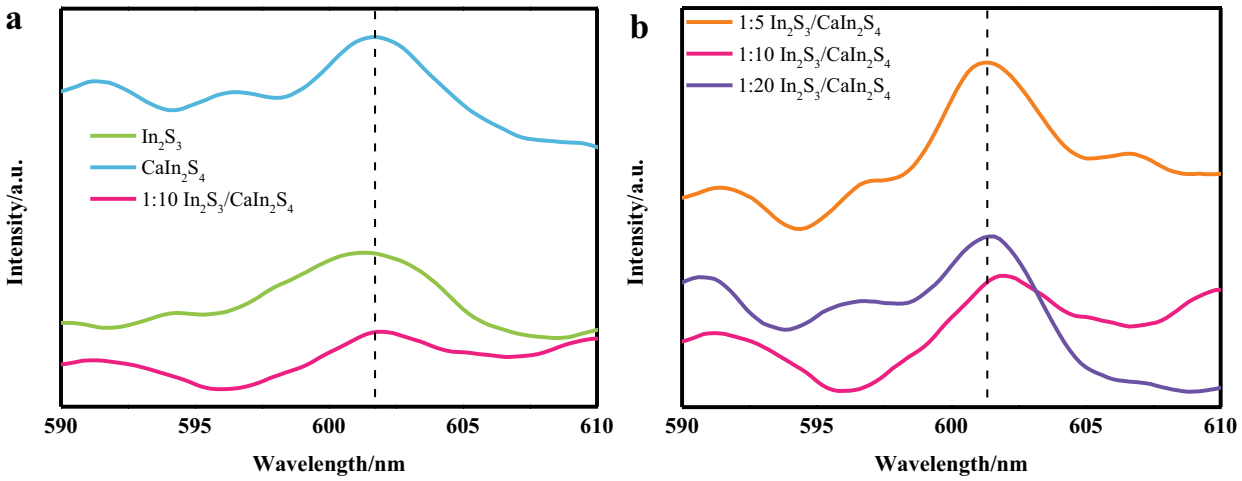

Fig. 6. Photoluminescence spectra of In_2S_3, $CaIn_2S_4$, and 1:10 $In_2S_3/CaIn_2S_4$ (a), photoluminescence spectra of $In_2S_3/CaIn_2S_4$ composites with different ratios (b) (The excitation wavelength is 400 nm).

and the degradation rate is very low, while the addition of $CaIn_2S_4$, In_2S_3, P25, and different proportions of $In_2S_3/CaIn_2S_4$, the degradation effect is significantly enhanced, among which the photocatalytic activity of 1:10 $In_2S_3/CaIn_2S_4$ is the strongest. In Fig. 7c, the direct photolysis, P25, $CaIn_2S_4$, In_2S_3 and 1:10 $In_2S_3/CaIn_2S_4$ (optimum photocatalyst) are sequentially enhanced after 180 min under visible light irradiation. The degradation effect of 1:10 $In_2S_3/CaIn_2S$ is obviously improved, and the as-prepared photocatalyst has an obvious degradation effect on MO under visible light irradiation.

Due to the difference in the bandgap energy of In_2S_3 and $CaIn_2S_4$, a synergistic effect occurs after the combination of the two components, thus improving their photocatalytic activity. It can be clearly seen from Fig. 7d that in the degradation experiments of different samples on the dye MO, $-\ln(C_t/C_0)$ is basically linear with the reaction time t, indicating that the degradation of methyl orange follows the pseudo-first-order reaction kinetics. After calculation, under visible light, the calculated rate constants of direct photolysis, P25, pure $CaIn_2S_4$, pure In_2S_3, and $In_2S_3/CaIn_2S_4$ are 9.09×10^{-5}, 4.35×10^{-4}, 4.51×10^{-3}, 6.25×10^{-3}, and 7.98×10^{-3} min^{-1}, respectively. Therefore, the photocatalytic activities of various photocatalysts under visible light irradiation are: 1:10 $In_2S_3/CaIn_2S_4$ > pure $CaIn_2S_4$ > pure In_2S_3 > P25 > direct photolysis. It can be seen from Fig. 7e the degradation rates of 1:10 $In_2S_3/CaIn_2S_4$ to methyl orange, rhodamine B, acid fuchsin, and methylene blue within 60 min. By contrast, $In_2S_3/CaIn_2S_4$ composite also has a certain universality to degrade different types of dyes under ultraviolet light irradiation. The degradation effect is excellent, and it has a bright application prospect.

In addition, it can be seen from Fig. 7f, through four recycling experiments, the stability and recyclability of the photocatalyst were evaluated by the degradation effect of the recovered photocatalyst on MO. The recycled photocatalyst is washed with water and alcohol, however, the degradation rate is still reduced in degree, since the adsorbed dye could not be removed from the photocatalyst, because it can't bear the high temperature calcination. It can be seen from Fig. 7g that after simulated sunlight irradiation for 210 min, 1:10 $In_2S_3/CaIn_2S_4$ has good activity in photocatalytic degradation and is obviously higher than other systems. In order to study the degradation efficiency of methyl orange by 1:10 $In_2S_3/CaIn_2S_4$ photocatalyst in various actual water environments, tap water, lake water and snow water were sampled in Qiqihar City, Heilongjiang Province, and the results were compared with the deionized water in Fig. 7h.

In order to investigate the photocatalytic hydrogen production ability of the as-prepared $In_2S_3/CaIn_2S_4$ composites, the photocatalytic hydrogen evolution experiment was carried out, as shown in Fig. 8a. From Fig. 8a, the photocatalytic hydrogen evolution ability of 1:10 $In_2S_3/CaIn_2S_4$ is significantly higher than that of P25. After compounding of monomer $CaIn_2S_4$ with slightly hydrogen-producing In_2S_3, the conduction band of the composite material $In_2S_3/CaIn_2S_4$ is more negative than that of H_2/H_2O (0.0 eV vs NHE). It means that the composites have a stronger reducing ability, thereby improving the hydrogen production capacity of the composite material.

3.8. Reaction mechanism

As we all know, the main principle behind photocatalytic degradation involves a semiconductor comprising a valence band (VB) and conduction band (CB) in its electronic structure. These bands have an energy gap between them called a bandgap. When illuminated by photons having energy ≥ bandgap energy, the electron present in the valence band is excited to the CB, generating a positively charged hole in the VB. Both hole and electron are strongly oxidizing and reducing species, respectively. When the hole and electron react with H_2O molecules, hydroxyl ($^{\bullet}OH$) and superoxide ($^{\bullet}O_2^-$) radicals are generated, which attack the organic dyes and convert them into non-hazardous compounds like CO_2 and H_2O [40]. To investigate the reaction mechanism of the as-synthesized photocatalyst, trapping experiments with $In_2S_3/CaIn_2S_4$ were carried out, and the results are shown in Fig. 8b. Adding EDTA-2Na and

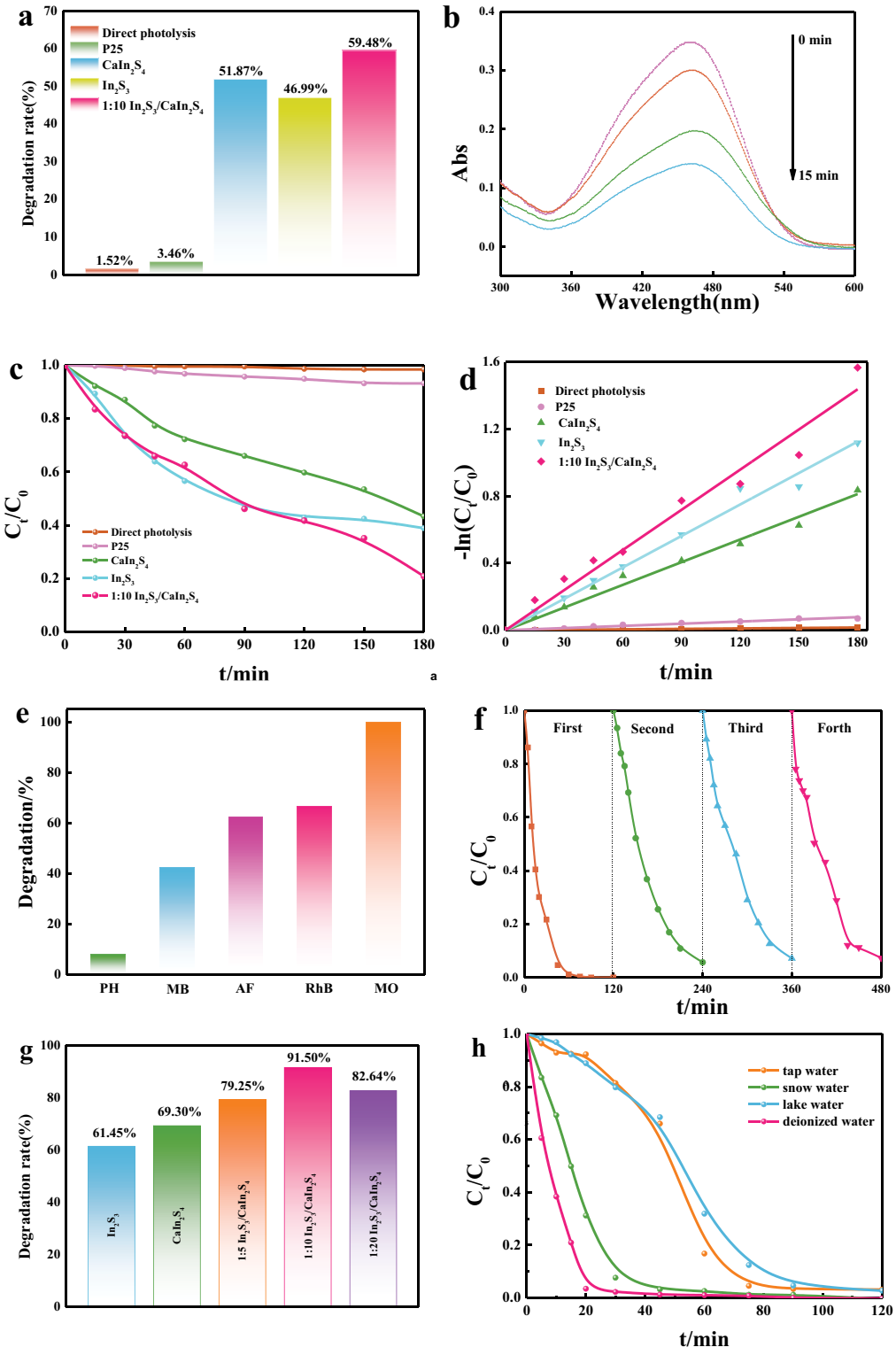

Fig. 7. Photocatalytic degradation profiles of methyl orange for different photocatalysts under ultraviolet light irradiation (t = 15 min) (a), absorption curve of 1:10 $In_2S_3/CaIn_2S_4$ for methyl orange under ultraviolet light (b), degradation results of methyl orange by different photocatalysts under visible light (t = 180 min) (c), kinetics profiles of methyl orange degradation with different photocatalysts (d), degradation results of 1:10 $In_2S_3/CaIn_2S_4$ for different organic pollutants under ultraviolet light (t = 60 min) (e), recycling experiments of 1:10 $In_2S_3/CaIn_2S_4$ under ultraviolet light (f), photocatalytic degradation profiles of methyl orange for different photocatalysts under simulated sunlight (t = 210 min) (g), photodegradation of different natural water matrices in Qiqihar City, Heilongjiang Province (h).

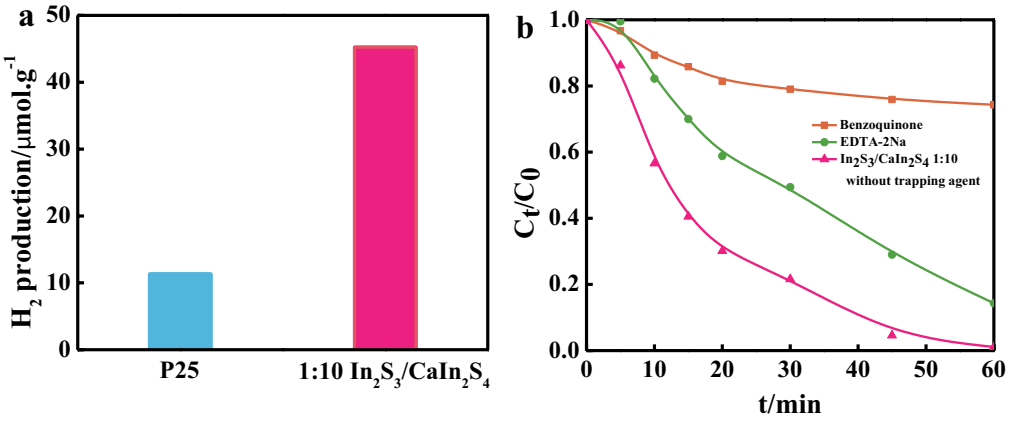

Fig. 8. Amounts of H_2 generated over 1:10 $In_2S_3/CaIn_2S_4$ and P25 (a), trapping experiment results of 1:10 $In_2S_3/CaIn_2S_4$ (b).

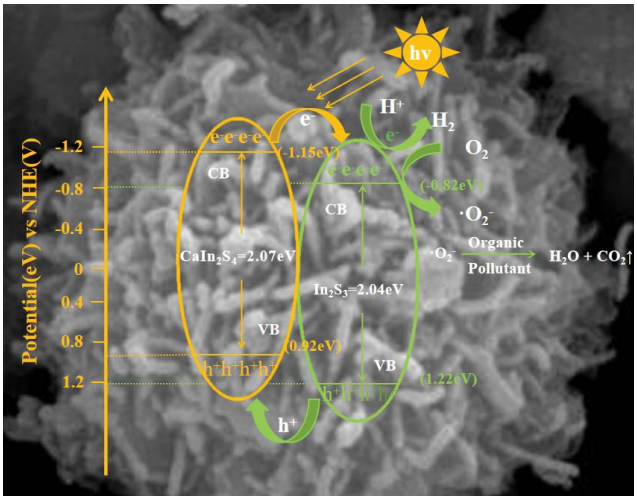

Fig. 9. Photocatalytic reaction mechanism of $In_2S_3/CaIn_2S_4$ composite.

p-benzoquinone as holes (h^+) and superoxide radicals ($^{\bullet}O_2^-$) to the reaction system, respectively. The reaction mechanism of photocatalytic degradation of MO by 1:10 $In_2S_3/CaIn_2S_4$ composite was explored. After adding EDTA-2Na and p-benzoquinone, the photocatalytic performance of 1:10 $In_2S_3/CaIn_2S_4$ was weakened to a certain extent, the results showed that superoxide radicals ($^{\bullet}O_2^-$) play a leading role in the photocatalytic reaction process.

Based on the results of the trapping experiment, a possible photocatalytic mechanism was proposed, as shown in Fig. 9.

According to the formula as follow:

$$E_{CB} = \chi - E_C - 0.5E_g \quad (2)$$

$$E_{VB} = E_{CB} + E_g \quad (3)$$

where χ represents the absolute electronegativity of the semiconductor, and it could be manifested as the geometric mean of electronegativity of combining elements, E_C refers to the scaling factor describing the redox level of the reference electrode to the vacuum (E_C = –4.5 eV for NHE). E_{CB} signifies the conduction band (CB) potential, E_{VB} refers to the valence band (VB) potential, and E_g is the bandgap of the semiconductor. The positions of the conduction band and valence band of In_2S_3 and $CaIn_2S_4$ are calculated, and the results are shown in Table 3.

Table 3
Conduction band and valence band potential of In_2S_3 and $CaIn_2S_4$

Sample	In_2S_3	$CaIn_2S_4$
E_{CB} (eV)	–0.82	–1.15
E_{VB} (eV)	1.22	0.92

Under illumination, the electrons of $CaIn_2S_4$ in the composite $In_2S_3/CaIn_2S_4$ are excited and transferred from the VB of $CaIn_2S_4$ to the CB of $CaIn_2S_4$, thus forming electron–hole pairs. At the same time, due to the close contact between In_2S_3 and $CaIn_2S_4$, photogenerated electrons can be rapidly transferred to the CB of In_2S_3 and react with H^+ to generate H_2. During the reaction process, the oxygen molecules adsorbed on the surface of the photocatalyst are further captured by photogenerated electrons and become reactive oxygen molecules (superoxide radical ($^{\bullet}O_2^-$)), which inhibit the electron–hole pair recombination to a certain extent and prolong the lifetime of the carrier. Capture experiments confirm the presence of $^{\bullet}O_2^-$, which can degrade and mineralize pollutants to CO_2 and H_2O [41,42].

4. Conclusion

$In_2S_3/CaIn_2S_4$ composites were synthesized by a programmed temperature hydrothermal method. The composites are mixed crystal phase of cubic phase $CaIn_2S_4$ and tetragonal phase β-In_2S_3, with rambutan-like morphology, large specific surface area, and large absorption in the visible region. The as-synthesized 1:10 $In_2S_3/CaIn_2S_4$ composites have a high degradation rate for organic pollutants with different structures, and the hydrogen production capacity is significantly higher than that of P25, indicating that $In_2S_3/CaIn_2S_4$ composites have certain application prospects of degrading wastewater and developing hydrogen energy.

Acknowledgements

This study was supported by the National Natural Science Foundation of China (21776144, 21376126), the Heilongjiang Provincial Natural Science Foundation of China (LH2021B031), the Fundamental Research Funds in Heilongjiang Provincial Universities of China (145109104), Scientific Research Foundation for Scholars funded by Zhejiang University of Technology (2022181010002), the Innovation Project of Qiqihar University Graduate Education (YJSCX2020037), Innovation and entrepreneurship training program for college students of Qiqihar University (202220232037), and the College Students' Innovative Entrepreneurial Training Program Funded Projects of Qiqihar University (202110232154).

Conflicts of interest

There are no conflicts to declare.

References

[1] A. Das, M.K. Adak, Photo-catalyst for wastewater treatment: a review of modified Fenton, and their reaction kinetics, Appl. Surf. Sci. Adv., 11 (2022) 100282, doi: 10.1016/j.apsadv.2022.100282.
[2] D.X. Gao, H.T. Yang, Z. Shu, The preparation of Ag@AgCl photocatalytic material based on the photocatalysis material CA^+ and degradation of tetracycline, J. Exp. Nanosci., 18 (2023) 2162509, doi: 10.1080/17458080.2022.2162509.
[3] K.F. Rodrigues, N.P. de Moraes, A.S. dos Santos, T.L. do Amaral Montanheiro, T.M.B. Campos, G.P. Thim, L.A. Rodrigues, D.D. Brunelli, Enhanced 4-chlorophenol degradation under visible and solar radiation through TiO_2/g-C_3N_4 Z-scheme heterojunction, Biointerface Res. Appl. Chem., 13 (2023) 1–18.
[4] H. Takashi, K. Jun, D. Kazunari, Recent advances in semiconductors for photocatalytic and photoelectrochemical water splitting, Chem. Soc. Rev., 43 (2014) 7520–7535.
[5] D. Kandi, S. Martha, K.M. Parida, Quantum dots as enhancer in photocatalytic hydrogen evolution: a review, Int. J. Hydrogen Energy, 42 (2017) 9467–9481.
[6] Y. Yang, S.H. Zhao, F.K. Bi, J.F. Chen, Y.X. Wang, L.F. Cui, J.C. Xu, X.D. Zhang, Highly efficient photothermal catalysis of toluene over Co_3O_4/TiO_2 p-n heterojunction: the crucial roles of interface defects and band structure, Appl. Catal., B, 315 (2022) 121550, doi: 10.1016/j.apcatb.2022.121550.
[7] Y. Yang, S.H. Zhao, F.K. Bi, J.F. Chen, Y.T. Li, L.F. Cui, J.C. Xu, X.X. Zhang, Oxygen-vacancy-induced O_2 activation and electron-hole migration enhance photothermal catalytic toluene oxidation, Cell Rep. Phys. Sci., 3 (2022) 101011, doi: 10.1016/j.xcrp.2022.101011.
[8] J.F. Chen, Y. Yang, S.G. Zhao, F.K. Bi, L. Song, N. Liu, J.C. Xu, Y.X. Wang, X.D. Zhang, Stable black phosphorus encapsulation in porous mesh-like UiO-66 promoted charge transfer for photocatalytic oxidation of toluene and o-dichlorobenzene: performance, degradation pathway, and mechanism, ACS Catal., 12 (2022) 8069–8081.
[9] R.F. Peng, S. Zhang, Y.Y. Yao, J.N. Wang, X.F. Zhu, R. Jiang, J.H. Zhang, W. Zhang, C.H. Wang, MOFs meet electrospinning: new opportunities for water treatment, J. Environ. Sci., 453 (2022) 139669, doi: 10.1016/j.cej.2022.139669.
[10] X.Q. Dai, L. Chen, Z.Y. Li, X.J. Li, J.F. Wang, X. Hu, L.H. Zhao, Y.M. Jia, S.X. Sun, Y. Wu, Y.M. He, CuS/$KTa_{0.75}Nb_{0.25}O_3$ nanocomposite utilizing solar and mechanical energy for catalytic N_2 fixation, J. Colloid Interface Sci., 603 (2021) 220–232.
[11] L. Chen, X.Q. Dai, X.J. Li, J.F. Wang, H.F. Chen, X. Hu, H.J. Lin, Y.M. He, Y. Wu, M.H. Fan, A novel Bi_2S_3/$KTa_{0.75}Nb_{0.25}O_3$ nanocomposite with high efficiency for photocatalytic and piezocatalytic N_2 fixation, J. Mater. Chem. A, 9 (2021) 13344–13354.
[12] S. Zheng, X.J. Li, J.Y. Zhang, J.F. Wang, C.R. Zhao, X. Hu, Y. Wu, Y.M. He, One-step preparation of MoO_3/ZnS/ZnO composite and its excellent performance in piezocatalytic degradation of Rhodamine B under ultrasonic vibration, J. Environ. Sci., 125 (2023) 1–13.
[13] Q.L. Zhang, P.F. Chen, L. Chen, M.F. Wu, X.Q. Dai, P.X. Xing, H.J. Lin, L.H. Zhao, Y.M. He, Facile fabrication of novel Ag_2S/K-g-C_3N_4 composite and its enhanced performance in photocatalytic H_2 evolution, J. Colloid Interface Sci., 568 (2020) 117–129.
[14] T.S. Natarajan, R.J. Tayade, Direct dual $CaIn_2S_4$/Bi_2WO_6 semiconductor nanocomposites with efficient inter-cross-sectional charge carrier transfer for enhanced visible light photocatalysis, J. Nanopart. Res., 23 (2021) 127, doi: 10.1007/s11051-021-05252-y.
[15] J.J. Ding, S. Sun, W.H. Yan, J. Bao, C. Gao, Photocatalytic H_2 evolution on a novel $CaIn_2S_4$ photocatalyst under visible light irradiation, Int. J. Hydrogen Energy, 38 (2013) 13153–13158.
[16] S.Y. Xu, J. Dai, J. Yang, J. You, J.Y. Hao, Facile synthesis of novel $CaIn_2S_4$/$ZnIn_2S_4$ composites with efficient performance for photocatalytic reduction of Cr(VI) under simulated sunlight irradiation, Nanomaterials, 8 (2018) 472, doi: 10.3390/nano8070472.
[17] J.J. Ding, W.H. Yan, S. Sun, J. Bao, C. Gao, Hydrothermal synthesis of $CaIn_2S_4$-Reduced graphene oxide nanocomposites with increased photocatalytic performance, ACS Appl. Mater. Interfaces, 6 (2014) 12877–12884.
[18] G.X. Cao, Y.B. Zhao, Z.S. Wu, Synthesis and characterization of In_2S_3 nanoparticles, J. Alloys Compd., 472 (2009) 325–327.
[19] X.L. Fu, X.X. Wang, Z.X. Chen, Z.Z. Zhang, Z.H. Li, Photocatalytic performance of tetragonal and cubic β-In_2S_3, for the water splitting under visible light irradiation, Appl. Catal., B, 95 (2010) 393–399.
[20] X.W. Wang, W.X. Liu, X.Q. Wang, D.H. Yu, H. Liu, Preparation of In_2S_3@TiO_2 nanobelt heterostructures with high UV-Visible light photocatalytic activities, Sci. Adv. Mater., 7 (2015) 479–488.
[21] Y. Fang, S.R. Zhu, M.K. Wu, W.N. Zhao, L. Han, MOF-derived In_2S_3 nanorods for photocatalytic removal of dye and antibiotics, J. Solid State Chem., 266 (2018) 205–209.
[22] P. Zhang, L.N. Zhang, E.L. Dong, X. Zhang, W. Zhang, Synthesis of $CaIn_2S_4$/TiO_2 heterostructures for enhanced UV-Visible light photocatalytic activity, J. Alloys Compd., 885 (2021) 161027, doi: 10.1016/j.jallcom.2021.161027.
[23] S. Yang, C.Y. Xu, B.Y. Zhang, L. Yang, S.P. Hu, L. Zhen, Ca(II) doped β-In_2S_3 hierarchical structures for photocatalytic hydrogen generation and organic dye degradation under visible light irradiation, J. Colloid Interface Sci., 491 (2017) 230–237.
[24] G.D. Liu, X.L. Jiao, Z.H. Qin, D.R. Chen, Solvothermal preparation and visible photocatalytic activity of polycrystalline β-In_2S_3 nanotubes, Cryst. Eng. Comm., 13 (2011) 182–187.
[25] Z. Zhou, Y.H. Li, K.L. Lv, X.F. Wu, Q. Li, J.M. Luo, Fabrication of walnut-like $BiVO_4$@Bi_2S_3 heterojunction for efficient visible photocatalytic reduction of Cr(VI), Mater. Sci. Semicond. Process., 75 (2018) 334–341.
[26] J. Singha, R.K. Soni, J. Kim, Photocatalytic β-In_2S_3 nanoflowers synthesized by thermal assembly of In_2S_3 nanosheets, J. Alloys Compd., 911 (2022) 165099, doi: 10.1016/j.jallcom.2022.165099.
[27] I.J. Badovinac, R. Peter, A. Omerzu, K. Salamon, I. Šarić, A. Samaržija, M. Perčić, I.K. Piltaver, G. Ambrožić, M. Petravić, Grain size effect on photocatalytic activity of TiO_2 thin films grown by atomic layer deposition, Thin Solid Films, 709 (2020) 138215, doi: 10.1016/j.tsf.2020.138215.
[28] J. Li, S.C. Meng, T.Y. Wang, Q. Xu, L.Q. Shao, D.L. Jiang, M. Chen, Novel Au/$CaIn_2S_4$ nanocomposites with plasmon-enhanced photocatalytic performance under visible light irradiation, Appl. Surf. Sci., 396 (2016) 430–437.
[29] Y.H. He, D.Z. Li, G.G. Xiao, W. Chen, Y.B. Chen, A new application of nanocrystal In_2S_3 in efficient degradation of organic pollutants under visible light irradiation, J. Phys. Chem. C, 113 (2009) 5254–5262.

[30] P. Srivastava, N.L. Saini, B.R. Sekhar, K.B. Garg, Core-level photoemission study on a Bi-2212 single crystal, Mater. Sci. Eng., B, 22 (1994) 217–221.
[31] R.W. Hewitt, N. Winograd, Oxidation of polycrystalline indium studied by X-ray photoelectron spectroscopy and static secondary ion mass spectroscopy, J. Appl. Phys., 51 (1980) 2620–2624.
[32] K. Okada, A. Kotani, B.T. Thole, Charge transfer satellites and multiplet splitting in X-ray photoemission spectra of late transition metal halides, J. Electron. Spectrosc. Relat. Phenom., 58 (1992) 325–343.
[33] M. Tekalgne, A. Hasani, Q.V. Le, T.P. Nguyen, K.S. Choi, CdSe quantum dots doped WS_2 nanoflowers for enhanced solar hydrogen production, Phys. Status Solidi A, 216 (2019) 1800853, doi: 10.1002/pssa.201800853.
[34] S. Jasbinder, J. Heo, J. Mackenzie, R.M. Almeida, XPS study of non-bridging Se atoms in As_2Se_3-Tl_2Se glasses, J. Non-Cryst. Solids, 101 (1988) 18–22.
[35] B. Silvia, Glossary of terms used in photochemistry, 3rd edition (IUPAC Recommendations 2006), Pure Appl. Chem., 79 (2007) 239–465.
[36] F.K. Bi, Z.Y. Zhao, Y. Yang, W.K. Gao, N. Liu, Y.D. Huang, X.D. Zhang, Chlorine-coordinated Pd single atom enhanced the chlorine resistance for volatile organic compound degradation: mechanism study, Environ. Sci. Technol., 56 (2022) 17321–17330.
[37] S.M. Sun, W.Z. Wang, L. Zhang, Facile preparation of three-dimensionally ordered macroporous Bi_2WO_6 with high photocatalytic activity, J. Mater. Chem., 22 (2012) 19244–19249.
[38] X.D. Zhang, Z.Y. Zhao, S.H. Zhao, S. Xiang, W.K. Gao, L. Wang, J.C. Xu, Y.X. Wang, The promoting effect of alkali metal and H_2O on Mn-MOF derivatives for toluene oxidation: a combined experimental and theoretical investigation, J. Catal., 415 (2022) 218–235.
[39] J.J. Ning, K.K. Men, G.J. Xiao, L.Y. Zhao, L. Wang, B.B. Liu, B. Zou, Synthesis, optical properties and growth process of In_2S_3 nanoparticles, J. Colloid Interface Sci., 347 (2010) 172–176.
[40] P. Singh, B. Mohan, V. Madaan, R. Ranga, P. Kumari, S. Kumar, V. Bhankar, P. Kumar, K. Kumar, Nanomaterials photocatalytic activities for wastewater treatment: a review, Environ. Sci. Pollut. Res., 29 (2022) 69294–69326.
[41] R.J. Guo, R. Tian, D.L. Shi, H. Li, H.H. Liu, S-Doped $ZnSnO_3$ nanoparticles with narrow band gaps for photocatalytic wastewater treatment, ACS Appl. Nano Mater., 12 (2019) 7755–7765.
[42] J. Kang, C.Y. Jin, Z.L. Li, M. Wang, Z.Q. Chen, Y.Z. Wang, Dual Z-scheme MoS_2/g-C_3N_4/$Bi_{24}O_31Cl_{10}$ ternary heterojunction photocatalysts for enhanced visible-light photodegradation of antibiotic, J. Alloys Compd., 825 (2020) 153975, doi: 10.1016/j.jallcom.2020.153975.